Research Article

Vickers microhardness and indentation creep studies for erbium-doped ZnO nanoparticles

S. Farhat[1] · M. Rekaby[2] · R. Awad[1]

Abstract

The effect of erbium (Er) doping on the structural, magnetic and mechanical properties of $Zn_{1-x}Er_xO$, with $0.00 \le x \le 0.10$, samples was studied using X-ray powder diffraction, M–H magnetic hysteresis and digital Vickers microhardness tester, respectively. The samples were prepared by wet chemical co-precipitation method. Vickers microhardness (H_v) measurements were carried out at different applied loads (0.25–10 N) and dwell times (t = 10–60 s) to study the mechanical performance of the samples. Experimental results of H_v were analyzed using Meyer's law, and modeled according to Hays–Kendall, elastic/plastic deformation, modified proportional specimen resistance (MPSR) and Indentation Induced Cracking models. It was observed that the MPSR model was the most appropriate model for describing the load independent microhardness data of Er-doped ZnO nanoparticle samples. Indentation creep behavior of $Zn_{1-x}Er_xO$ samples was studied at room temperature by measuring the variation of H_v with the dwell times (t = 10–60 s) at fixed applied loads F = 1, 5 and 10 N, respectively. The results showed that Er-doped ZnO nanoparticles samples possessed grain boundary sliding and dislocation climbs at low loads followed by dislocation creep for higher loads within the operative creep mechanism.

Keywords Er-doped ZnO nanoparticles · Co-precipitation · XRD · Vickers microhardness · Indentation creep

1 Introduction

Zinc oxide (ZnO) is a one of the promising and technologically interesting semiconducting material due to its perfect properties such as resistivity control over the range of 10^{-4}–10^{5} Ωcm [1, 2], excellent chemical and thermal stability, low cost, non-toxicity, abundance in nature, high direct band gap of 3.37 eV, large exciton binding energy (60 meV) and good mechanical strength [3]. Zinc oxide crystallizes in a wurtzite hexagonal structure and exhibits n-type conductivity due to residual donors [4]. On the other hand, the wet chemical co-precipitation method has become very attractive for the preparation of nanomaterial over other methods because it proved to be simple, economical, time saving and effective for large scale production [5]. The obtained products have good homogeneity and high purity [6]. The particle size and composition are easy to be controlled [7] with the production of monodisperse samples [8] and the reaction temperature needed in this method is relatively low [9]. Despite all their advantages, some reports [10] state one noticeable disadvantage of the co-precipitation method is the large amount of adsorbed water present in the prepared nanoparticles affecting the spectral properties of the synthesized nanoparticles, as well as their luminescent characteristics [11, 12]. Another disadvantage of the co-precipitation method is caused by the fast growth of nanoparticles in aqueous solution causing the lattice to capture water molecules as it was reported by Tada et al. [13] and Alakshin et al. [14]. Many literatures [15–18] studied the electrical, magnetic and optical properties of ZnO, however a few studies can be found about their

---

✉ S. Farhat, samahfarhat2016@hotmail.com; saf286@student.bau.edu.lb | [1]Physics Department, Faculty of Science, Beirut Arab University, Beirut, Lebanon. [2]Physics Department, Faculty of Science, Alexandria University, Alexandria, Egypt.

SN Applied Sciences (2019) 1:546 | https://doi.org/10.1007/s42452-019-0559-4

Received: 15 January 2019 / Accepted: 3 May 2019 / Published online: 11 May 2019

mechanical properties which are relevant to the strength of these materials. Doping may significantly improve the internal structure and mechanical properties of the material [19–22]. In fact, nanomaterials may be distorted to some extent when they are incorporated in a wide variety of nanodevices [23]. So, a detailed investigation of their mechanical properties is a key step prior to any practical application. In particular, the importance of studying the mechanical properties of this nano ZnO compound such as microhardness, elastic modulus, yield strength, fracture toughness and brittleness index is due to the use of it in many applications such as electrical varistors, transparent high power electronics, surface acoustic wave devices, window materials for display, spintronic [22], nanoelectromechanical systems (NEMS) [24], nanosensors [25, 26] and nanogenerators [27, 28]. The indentation creep test provides a simple, quick and non-destructive method of investigating the mechanical properties of solids. It also gives information about the time dependent flow of materials [29–32]. This test is considered as an effective technique because all the creep information are recorded using the same sample which reduces the effort for sample preparation and permits to avoid the sample to sample variation in property [33]. Moreover, the investigation of the creep behavior is essential to evaluate the mechanical reliability when the nanodevices are used under long-term stress conditions. The mechanical reliability will determine the long-term stability and performance for many of the nanodevices [23]. Lin et al. [34] investigated the nanoscale creep behavior of single-crystal ZnO because it is usually fabricated into low-dimensional piezoelectric devices. They found that creep strain is mainly controlled by the interfacial diffusion between the nanoindenter tip and the test sample. Asikuzun et al. [35] investigated the effects of Al and Mg doping on the structural and mechanical properties of $Zn_{0.90}Mg_{0.10-x}Al_xO$ nanoparticles prepared by sol–gel technique. H_v values were decreased with increasing the Al concentration and the applied loads. The plateau region is reached around about 1.5 N for the samples. Hays–Kendall model was the best model to describe the micromechanical properties of the Al/Mg co-doped ZnO nanoparticles exhibiting ISE behavior. Arda et al. [22] synthesized polycrystalline nanoparticle powders of $Zn_{0.94}Mg_{0.01}TM_{0.05}O$ (TM = Ni, Co, Mn and Cr) using the sol–gel technique. The experimental results of H_v obeyed the normal ISE behavior. Moreover, $Zn_{0.94}Mg_{0.01}TM_{0.05}O$ showed a gradual decrease in the values of Vickers microhardness when doped with (TM = Ni, Co, Mn and Cr), respectively. Hays–Kendall approach was considered to be the most suitable model explaining the mechanical behavior of the $Zn_{0.94}Mg_{0.01}TM_{0.05}O$ samples.

This research aims to explore the effect of erbium doping in order to improve the mechanical properties of nano ZnO samples through Vickers microhardness measurements and indentation creep experiments. For this purpose, nanoparticles samples of $Zn_{1-x}Er_xO$ with $0.00 \le x \le 0.10$ were prepared by wet chemical co-precipitation method. The experimental data of Vickers microhardness were analyzed according to different models and the operative creep mechanisms were specified by calculating the values of the stress exponents for the prepared samples.

2 Experimental techniques

$Zn_{1-x}Er_xO$ nanoparticles were prepared using the wet chemical co-precipitation method. First, the needed amounts, according to stoichiometric ratios, of Zinc chloride ($ZnCl_2$) and erbium (III) chloride hexahydrate ($ErCl_3 \cdot 6H_2O$) were weighed and mixed with distilled water by a magnetic stirrer. Next, 4.0 M sodium hydroxide solution (NaOH) was added to obtain a basic mixture with pH of 12 approximately. Then, washing and filtration of the products were applied by adding distilled water to reach a neutral medium having a pH around 7. After that, heating at 60 °C for 2 h was carried out with continuous and constant stirring rate and then drying at 100 °C for 18 h took place to remove water. The final step was the calcination stage at 550 °C for 4 h in order to improve the crystallinity of the prepared samples. The obtained nano-powders were characterized by X-Ray powder diffraction measurements at room temperature using Bruker D8 advance powder diffractometer with Cu–K_α radiation ($\lambda = 1.54056$ Å) in the range $25° \le 2\theta \le 75°$. Magnetic measurements were carried out at room temperature using a vibrating sample magnetometer (Lake Shore 7410) having temperature range capability from 4.2 to 1273. To apply the Vickers microhardness tests, the powder was pressed using a hydraulic press in the form of a disc (1.5 cm in diameter and about 0.3 cm in thickness). The discs were heated in a tube furnace at 800° C for 4 h then cooled with a rate of 4 °C per minute. The Vickers microhardness of the prepared samples was measured in air using a digital microhardness tester (MHVD-1000IS) at room temperature. The applied loads range from (0.25 N to 10 N) for dwell times (t = 10–60 s). The mean value of three readings taken at different locations of the sample's surface was calculated to ensure the accuracy and the reliability of the measured values of Vickers microhardness taking into consideration that traces should not overlap. Indentation creep measurements were performed at different dwell times (t) and at fixed applied loads F = 1, 5 and 10 N, respectively.

3 Results and discussion

3.1 Structural analysis

XRD patterns of $Zn_{1-x}Er_xO$ nanoparticles with $0.00 \le x \le 0.10$ were discussed in our previous study [36]. The lattice parameters (a and c) and the average crystallite sizes (D) of $Zn_{1-x}Er_xO$ nanoparticles were calculated using the least square method and Debye–Scherrer's relation, respectively [36]. The particle sizes are found to be in the range of 22.9–36 nm.

3.2 Magnetic measurements

Magnetic hysteresis of $Zn_{1-x}Er_xO$ nanoparticles were recorded at room temperature and the results are plotted in Fig. 1a–c for x = 0.00, 0.01 and 0.08, respectively. The pure ZnO nanoparticles display room-temperature ferromagnetism (RTFM) behavior, which may be caused by some defects at the surface, interface, and grain boundary [37] or to lattice defects such as oxygen vacancy (V_o) or zinc interstitial (Zn_i) in pure ZnO nanoparticles [38]. Also, a diamagnetic and paramagnetic contribution appear in the hysteresis loop of pure ZnO sample at about 0.8 Tesla as M decreases with the increasing of H. This indicates the surface and ligand induced defects [39].The samples with x = 0.01 exhibits a room temperature ferromagnetism which may be caused by the substitution of Er^{3+} in Zn^{2+} sites rather due to the formation of any ferromagnetic secondary phase. Similar results were obtained by Chen et al. [40] for Er-doped ZnO thin films prepared by coupled plasma enhanced physical vapor deposition. They reported that because the Er_2O_3 powder has a paramagnetic property, it is logical to consider that the observed room temperature ferromagnetism is the intrinsic property of Er-doped ZnO films, and the ferromagnetism is a result of the substitution of Er^{3+} in Zn^{2+} sites. The bound magnetic polaron (BMP) model [41] can also be a logical explanation of the observed ferromagnetism in x = 0.01 sample. The sample with x = 0.08 exhibit an antiferromagnetic behavior which may be due to the increasing number of oxygen vacancies at high doping concentration of erbium causing a quenching of surface defects or shallow donors, as a result the AFM behavior predominates in this sample [42]. The values of the saturation magnetization (M_s), the retentivity (M_r) and coercivity (H_c) which are obtained from the hysteresis loops of each sample are tabulated in Table 1. It can be noticed from Table 1 that M_s and M_r follow nearly the same trends of variation with increasing doping concentration. While, H_c decreases with increasing Er^{3+} content. This is maybe due to the decrease in the nonmagnetic zinc cations at the expense of an increase in Er^{3+} content leading to a smaller anisotropy [43].

3.3 Vickers microhardness

Vickers microhardness (H_v) for erbium doped ZnO nanoparticles ($Zn_{1-x}Er_xO$) with $0.00 \le x \le 0.10$ is calculated according to the following relation [44]:

$$H_v = 1854.4\left(\frac{F}{d^2}\right)(\text{GPa}) \tag{1}$$

where F is the applied load in Newton and d is the average diagonal length of indentation in μm. Figure 2 shows the variation of room temperature H_v with the applied load (F), at loading time t = 60 s for x = 0.00, 0.02, 0.06 and 0.10. The variation can be analyzed into two regimes: a load dependent regime that appears at low applied loads

Table 1 The variation of M_s, M_r and H_c as a function of x

x	M_s (emu/g)	M_r (emu/g)	H_c (G)
0.00	0.049	0.018	441.34
0.01	0.028	0.004	230.34
0.08	0.637	0.018	151.46

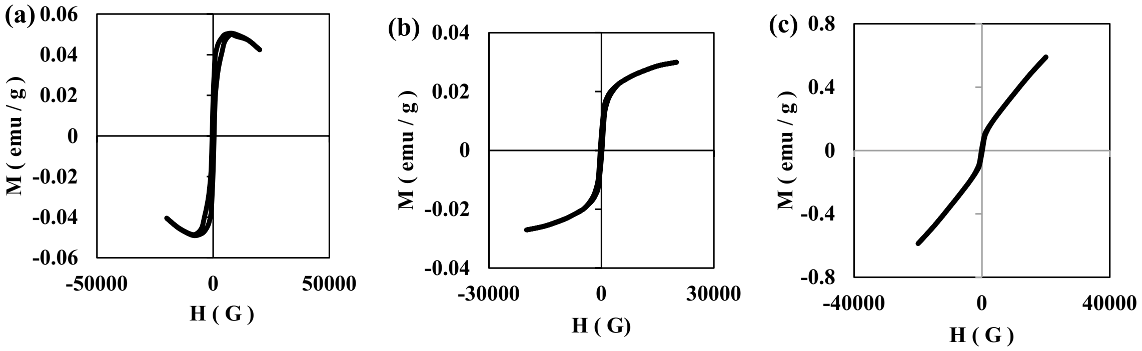

Fig. 1 M–H hysteresis loop for $Zn_{1-x}Er_xO$ nanoparticles for **a** x = 0.00, **b** x = 0.01 and **c** x = 0.08

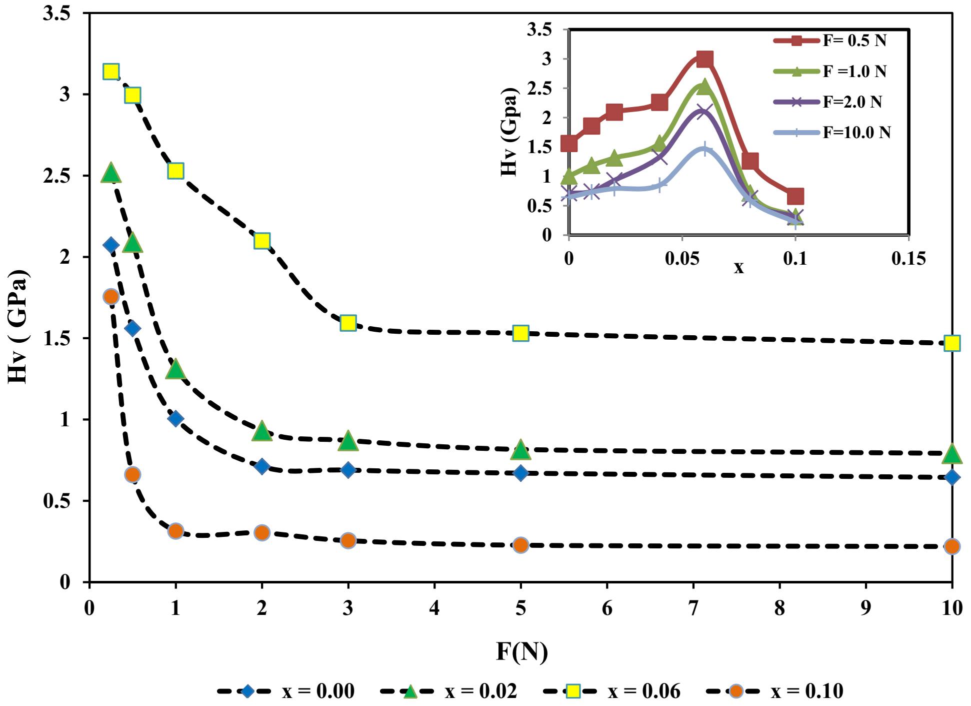

Fig. 2 Variation of experimental H_V for x = 0.00, 0.02, 0.06 and 0.10 as a function of different applied loads for $Zn_{1-x}Er_xO$ samples at a dwell time of 60 s. The inset shows the variation of H_V with x for F = 0.5, 1.0, 2.0 and 10.0 N

F < 3 N, where H_v decreases rapidly as the applied load increases and a load independent regime (almost plateau) that starts at higher loads for F > 3 N. This behavior is known as indentation size effect (ISE). At small loads, the indenter impacts only surface layers, while at higher loads, effect of inner layers becomes predominant as the penetration depth of the indenter increases. As a result, as the applied load increases, H_v values stay almost constant [45]. Siddheswaran et al. [19] synthesized pure, Co and Al co-doped ZnO powders by combustion method. The powder samples are uni-axially pressed into cylindrical discs and sintered at 1000 °C for 2 h. The grain sizes range from 0.5 to 3 µm. The recorded H_v values for pure ZnO were equal to 1.30, 1.55 and 1.42 GPa approximately at applied loads F of 1, 5 and 10 N, respectively, and a loading time of 10 s. In our study, H_v values for pure ZnO nanoparticles at a loading time of 10 s are 1.39, 0.86 and 0.79 GPa at F = 1, 5 and 10 N, respectively. It can be noticed from the comparison, that for F = 1 N the H_v values recorded in the micro and the nano scales are approximately equal. While, for higher loads, H_v values for nano-ZnO are lower than that recorded in Siddheswaran et al. work [19]. This difference may be due to the preparations methods, sintering temperatures and the differences in grain sizes. The inset of Fig. 2 displays the variation of H_v as a function of erbium doping content (x) at various applied loads F = 0.5, 1.0, 2.0 and 10.0 N. It was found, for all the applied loads (F), that H_v increases with increasing the Er-substitution content up to x = 0.06, then it decreases with the further increase in x. The increase in H_v with x can be attributed to the presence of Er in the ZnO lattice improving the connectivity among the grains. While, the drop of H_v with the further increase in x may be due to the separation of phases where erbium oxide (Er_2O_3) impurity migrates out the ZnO lattice and a secondary phase appears for x > 0.06 as it was confirmed in XRD analysis [36]. Figure 3 shows the effect of Er content (x) on the crystallite size (D) and on the values of Vickers microhardness (H_v) of $Zn_{1-x}Er_xO$ nanoparticles. Up to x = 0.04, H_v increases with decreasing crystallite size following regular Hall–Petch behavior [46] given by the following equation [47]:

$$H(D) = H_0 + K_{H-P} D^{-1/2} \tag{2}$$

H_0 and K_{H-P} are denoted as the lattice friction stress and the Hall–Petch constant, respectively. In Fig. 4, a plot of

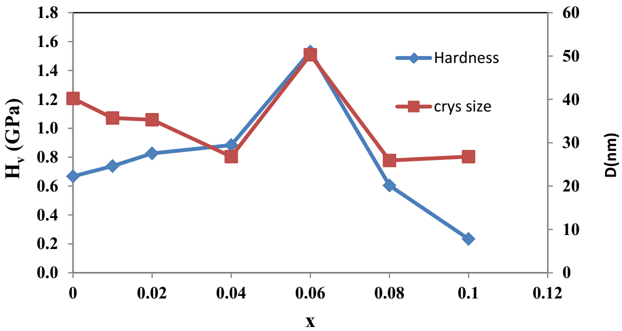

Fig. 3 Effect of Er content (x) on the crystallite size (D) and Vickers microhardness (H_v) of $Zn_{1-x}Er_xO$ nano samples

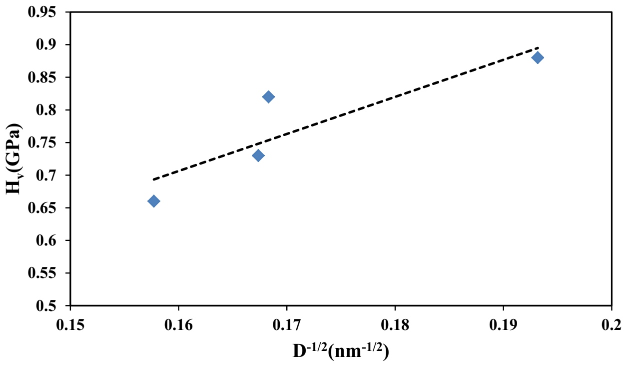

Fig. 4 Plot of the hardness (H_v) versus $D^{-1/2}$ for $Zn_{1-x}Er_xO$ nanoparticles, $0.00 \le x \le 0.04$

the hardness (H_v) versus $D^{-1/2}$ for $Zn_{1-x}Er_xO$ nanoparticles, $0.00 \le x \le 0.04$, is shown. The dashed line in Fig. 4 is a fit to the experimental data using the Eq. (2) with the form of $H(D) = -0.20 + 5.68D^{-1/2}$. The Hall–Petch constant K_{H-P} in our study is equal to 5.68 GPa $nm^{1/2}$ lower than that of nanocrystalline Zn (9.83 GPa $nm^{1/2}$) [48]. Moreover, K_{H-P} for pure copper (5.00 MPa $mm^{1/2}$) and pure Ni (4.90 MPa $mm^{1/2}$) [49] are close to the value in our work. While, for ZnO thin films annealed at various temperatures, K_{H-P} was equal to 38.4 GPa $nm^{1/2}$ indicating the effectiveness of the grain boundary to hinder the dislocation movements as was reported by Yen et al. [50].

However, deviation from Hall–Petch behavior is observed for $Zn_{1-x}Er_xO$ nanoparticles, $0.06 \le x \le 0.10$, samples where H_v decreases with further decrease in crystallite size. Bahadur et al. [51] studied the effect of Cobalt doping on the mechanical properties of ZnO thin films. They also related the change in the trends of microhardness values to the grain size. The microhardness in the samples of $Zn_{1-x}Co_xO$ nanoparticles increased up to $x = 0.05$ following the regular Hall–Petch relation. For $x > 0.05$, the separation of phases leads to a decrease in microhardness values and the inverse of Hall–Petch relation was observed.

It can be noticed from the obtained experimental data that the minimum indentation length is 12.15 µm at F = 25 N and a loading time of 60 s for the 6% erbium content sample. While the maximum indentation length is 290 µm at a load of 1000 N and loading time 60 s for the sample with 10% erbium doping. Li et al. [52] proposed that nanoindentation depth should never exceed 30% of films thickness. Penetration depth (h) is related to the indentation length (d) by the following formula (d = 7 h). The 30% of the sample thickness in our study is equal to 900 µm; the maximum indentation depth is 41.42 µm which does not exceed 900 µm, so our results are in agreement with Li et al. [52] suggestion. In other report [53], they stated that the thickness of the sample should be equal at least ten times the indentation depth.

3.3.1 Analyses and modeling

The obtained experimental microhardness data were analyzed and modeled according to Meyer's law, Hays–Kendall, elastic/plastic deformation, modified proportional specimen resistance and indentation induced cracking models which are described by the Eqs. (3)–(7), respectively [54–58]:

$$F = A\,d^n \tag{3}$$

$$F = W_{HK} + A_1 d^2 \tag{4}$$

$$F = A_2 \left(d + d_e\right)^2 \tag{5}$$

$$F = \alpha_2 + \alpha_3 d + \alpha_4 d^2, \tag{6}$$

$$H_v = \lambda_1 K_1 \left(\frac{F}{d^2}\right) + K_2 \left(\frac{F^{5/3}}{d^3}\right) \tag{7}$$

A is a constant, denoting the load required to start a unit indentation, n is Meyer's index, W_{HK} is the minimum applied load needed to start an indentation, A_1 is a load independent constant, d_e is the elastic component, A_2 is a constant, α_2 corresponds to the minimum applied load needed to produce an indentation or it is a constant related to the surface residual stresses associated with surface machining and polishing. α_3 and α_4 are related to energy dissipated in creating a new surface of unit area and in producing a permanent deformation of unit volume, respectively. λ_1, K_1 and K_2 are constants. The constant K_2 depends on the applied load F while K_1 is a geometrical conversion factor whose value depends on the indenter geometry. Figure 5a–e display the experimental microhardness data for $Zn_{1-x}Er_xO$ nano-particles samples with $0.00 \le x \le 0.10$ fitted according to Meyer's law, Hays and Kendall, elastic/plastic deformation, modified proportional specimen resistance and indentation induced cracking models, respectively. The fitting parameters for all models are listed in Table 2. The True microhardness values obtained from Hays–Kendall, EPD, MPSR and IIC approaches are calculated [45, 59] according to Eqs. (8)–(11), respectively, and the values are listed in Table 3.

$$H_{HK} = 1854.4 \times \frac{F - W_{HK}}{d^2} \tag{8}$$

$$H_{EPD} = 1854.4 \times \frac{F}{\left(d + d_e\right)^2} \tag{9}$$

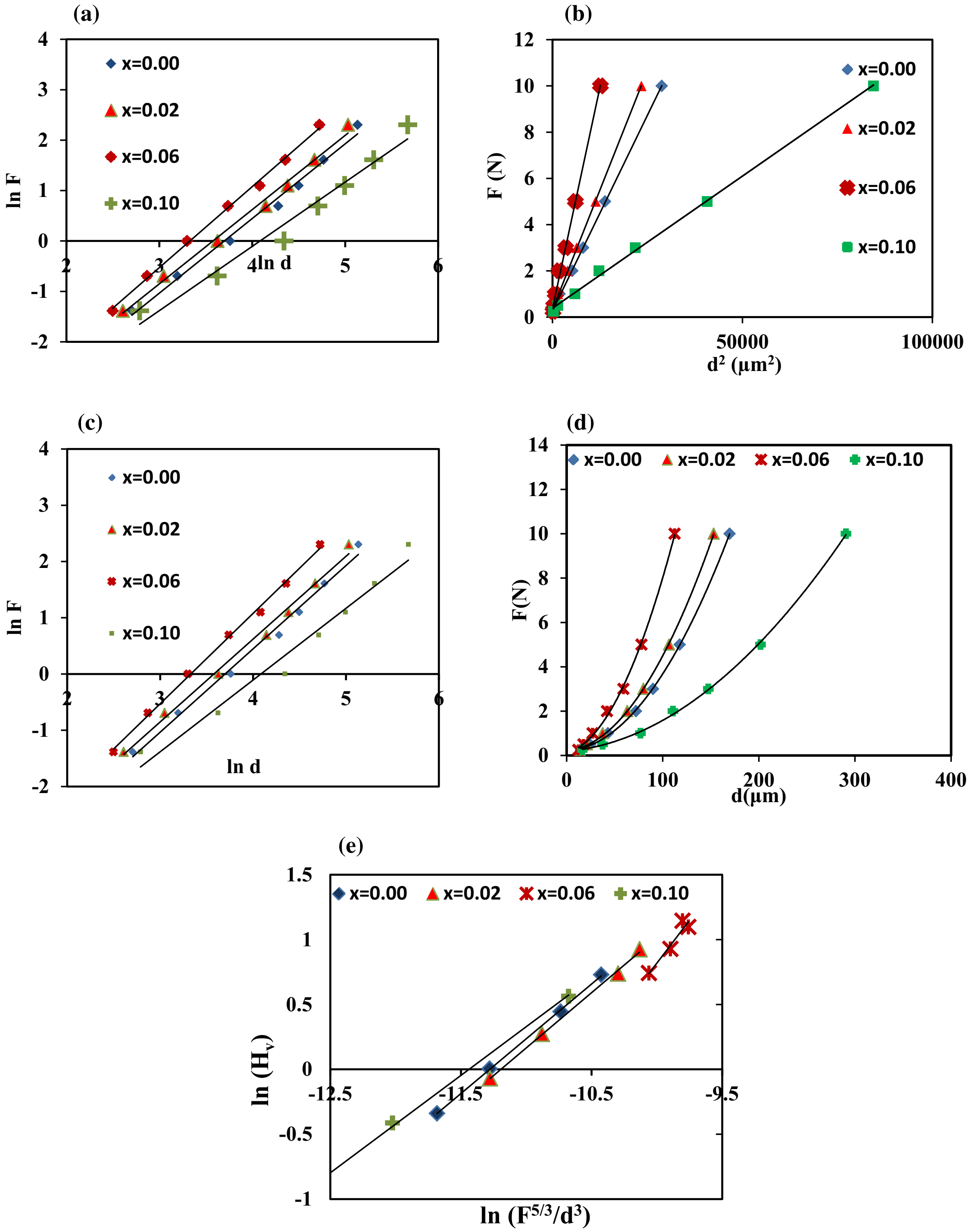

Fig. 5 **a** ln F against ln d according to Meyer's law, **b** variation of F with d^2 according to Hays–Kendall model, **c** plot of $F^{1/2}$ versus d according to EPD model, **d** graph of F against d according to MPSR model and **e** variation of ln (H_v) against ln ($F^{5/3}/d^3$) according to IIC model

$$H_{MPSR} = 1854.4 \times \frac{\alpha_2 + \alpha_3 d + \alpha_4 d^2}{d^2} \tag{10}$$

$$H_{IIc} = k\left(\frac{F^{5/3}}{d^3}\right)^m \tag{11}$$

It can be noticed that Eq. 11 is the second part of Eq. 7 and it is used because $Zn_{1-x}Er_xO$ nano-samples are brittle materials. *k* and the exponent m are constants that are load independent. In fact, all the samples have Meyer index values less than 2 and the values of the index m are

Table 2 Fitting parameters of Meyer's law, Hays and Kendall, elastic/plastic deformation, modified proportional specimen resistance and indentation induced cracking models for $Zn_{1-x}Er_xO$ nano-particles

X	Meyer's law		Hays and Kendall Model		Elastic plastic deformation model		Modified proportional specimen resistance model			Indentation induced cracking model	
	n	A (GPa)	$A_1 \times 10^{-4}$ (GPa)	W_{HK} (N)	$A_2 \times 10^{-4}$ (GPa)	d_e (µm)	α_2 (N)	$\alpha_3 \times 10^{-3}$ (N/µm)	$\alpha_4 \times 10^{-4}$ (N/µm^2)	m	K ($N^{(3-5 m)/3}/mm^{(2-3 m)}$)
0.00	1.48	0.0041	3.39	0.27	2.89	14.62	0.225	1.530	3.30	0.843	13,507.5
0.01	1.46	0.0049	3.84	0.22	3.20	13.78	0.339	−3.828	4.05	0.825	10,790.2
0.02	1.47	0.0051	4.14	0.31	3.49	14.36	0.220	3.318	3.95	0.851	13,569.7
0.04	1.46	0.0058	4.39	0.41	3.64	16.27	0.210	7.375	3.95	0.901	22,048.5
0.06	1.60	0.0047	7.67	0.35	6.67	9.72	0.121	10.715	6.83	1.039	76,879.9
0.08	1.49	0.0034	3.12	0.19	2.69	12.64	0.225	−0.746	3.16	0.819	10,807.5
0.10	1.27	0.0054	1.14	0.38	0.94	32.80	0.193	3.615	1.03	0.750	5329.9

Table 3 Variation of the experimental microhardness at the plateau region, and the calculated microhardness according to HK, EPD, MPSR and IIC models versus the doping content (x)

x	H_v (GPa) (experimental) plateau region	H_{HK} (GPa)	H_{EPD} (GPa)	H_{MPSR} (GPa)	H_{IIC} (GPa)
0.00	0.667	0.62	0.52	0.66	0.75
0.01	0.738	0.70	0.58	0.74	0.83
0.02	0.826	0.77	0.64	0.83	0.91
0.04	0.883	0.80	0.65	0.90	0.93
0.06	1.530	1.41	1.20	1.56	1.60
0.08	0.604	0.57	0.49	0.60	0.70
0.10	0.233	0.21	0.17	0.23	0.26

greater than 0.6 for all samples. This means that all the samples obey the normal ISE trend [59, 60]. In addition, the phenomenon of normal ISE behavior ($n < 2$) is assumed to be related to geometrically necessary dislocations (GNDs). Thus, it can be believed that dislocations mainly control the deformation of materials with lower n value more than that for higher n values, which explains the high hardness at low loading conditions [61, 62]. Some reports [61] states that the smaller n value indicates that the size effect becomes more dominant and the strain gradient increases due to the formation of a large population of sessile dislocations. Likewise, the approximate decrease in n values from 1.48 for the pure sample to 1.27 for $x = 0.10$ implies that the samples exhibit more ISE behavior with increasing Er-doping content [63]. On the other hand, Meyer's index is also related to the lattice perfection, with larger value signifying larger lattice damage [64]. As a result, the increasing value of n between $x = 0.00$ and $x = 0.06$ is due the lattice damage resulting from the larger Er^{3+} ions (0.88 Å) substituting Zn^{2+} ions (0.74 Å) in ZnO lattice. While, for erbium content above 0.06, the decrease in Meyer's index may imply that the lattice damage is recovered due to the migration of Er^{3+} ions out of ZnO lattice to form Er_2O_3 impurity resulting in a decrease of their destructive effect on the lattice. Moreover, it is important to notice that the material is regarded as a hard material if n is between 1.0 and 1.6, while for $n > 1.6$ the material is considered as a soft material [65]. In our case, the n values are between 1.27 and 1.60 implying that our samples are hard materials. But finally, some reports [66] considered that despite all their attempts, researchers did not find a satisfactory physical meaning of n and A. Asikuzun et al. [67] found a normal ISE for (Co/Mg) doped ZnO nano-crystalline samples only for samples with Co > Mg ratio. While, in samples with Mg > Co ratio a reverse indentation size effect (RISE) was observed. It can be noticed from Table 2 that the parameters A_1, A_2 and $_4$ which measured the load independent microhardness obtained from Hays–Kendall, EPD and MPSR models, respectively, increase up to $x = 0.06$, then they decrease with further increase in x. These trends confirm that load-independent microhardness values for $Zn_{1-x}Er_xO$ nano-samples are consistent with the trends of measured microhardness values obtained experimentally. W_{HK}, d_e and α_2 do not show a systematic trend of variation, but they can be analyzed as follows: W_{HK} values are almost greater than the lowest applied load used in our work (0.25 N), and they have positive values. This fact implies that the applied loads are enough to produce both elastic and plastic deformations and an elastic relaxation occurs on the sample's surface after the removal of the indenter

[59, 68]. The positive values of d_e and α_2 confirm the results obtained from Hays–Kendall model, showing that there is elastic deformation in $Zn_{1-x}Er_xO$ nano-samples along with plastic deformation and the ISE behavior dominates [59]. The obtained values from Eqs. (8–11) are compared with the experimental data in Fig. 6. It is clear, from Table 3 and Fig. 6, that the calculated Vickers microhardness from HK and EPD models are less than those of the experimental values in the plateau region with a deviation of 7.3% and 28.5%, respectively. While the values calculated from the IIC approach are almost greater than the experimental values and the deviation of this model is 9.8%. The calculated deviation of the MPSR model is 1% which is the lowest deviation among all the models, implying that the MPSR model is the most adequate model for describing the mechanical behavior of $Zn_{1-x}Er_xO$ nano-particles. The validity of the MPSR model for our data is understood since this model considers that the microhardness measurements are affected by machining induced residually stressed surface represented by α_2 which can be considered as a specimen constant rather than a material constant. So, the ISE behavior in our work could be caused by finishing process (grinding, pressing) which create plastic deformation and introduce cracks in the material adjacent to the surface [69]. Additionally, α_2 values in our study are relatively small which can be considered as logical estimates of surface stress for samples subjected to accurate finishing process (grinding–pressing). In the other models, the finishing process is not taken into consideration and does not have a correction term like α_2. Anas et al. [68] considered that the PSR model (which is the original law with respect to the MPSR model) was valid for their work because there is absence of elastic recovery after load removal while the other models (Hays–Kendall and EPD) adopt a point of view of elastic recovery after load removal.

3.4 Indentation creep

Indentation creep experiments were carried out to investigate the power law indentation creep behavior of erbium doped ZnO nanoparticles ($Zn_{1-x}Er_xO$) with $0.00 \le x \le 0.10$. Figure 7 displays the room temperature variation of H_v with the dwell time (t) at fixed applied loads F = 1, 5 and 10 N, respectively, for x = 0.02 and x = 0.10 samples. It is obvious from the Fig. 7 that the microhardness decreases with increasing the dwell time and two stages of transitions are observed. The first stage dominates for dwell time t < 40 s where there is a sharp decrease in $H_V - t$ curves, followed by a second transition stage that appears at

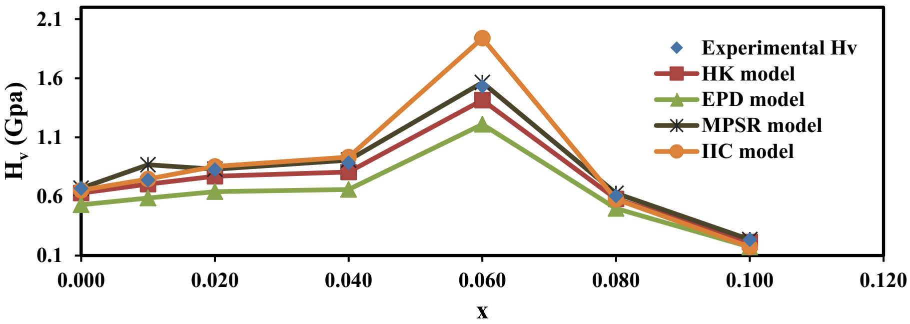

Fig. 6 The deviation between the measured and calculated Vickers microhardness for $Zn_{1-x}Er_xO$ nano-particles according to different models

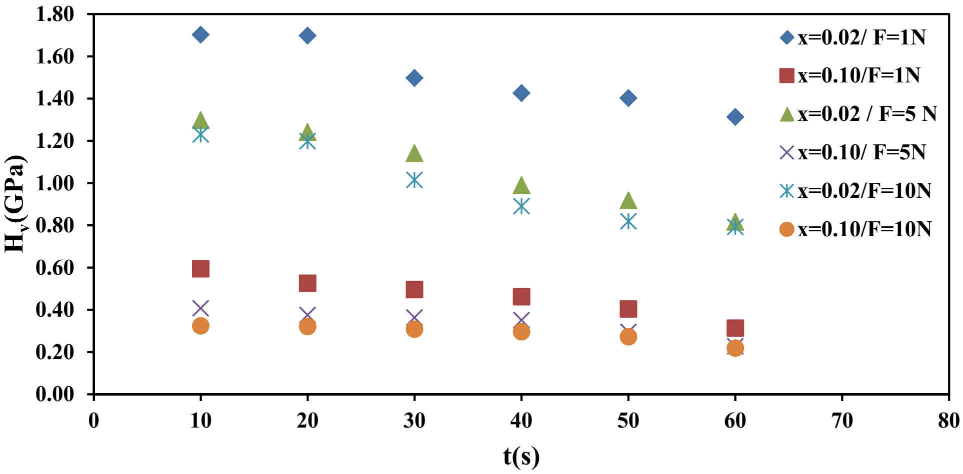

Fig. 7 Variation of hardness (H_V) as a function of dwell time (t) at constant loads 1, 5 and 10 N for x = 0.02 and x = 0.10 samples

dwell time t > 40 s where there is a linear decrease in the microhardness, with a lower decreasing rate, as the dwell time increases. The $H_v - t$ behavior, confirming the basis of the penetration depth of the indenter and reflects the characteristic behavior between H_v and t [70]. Also, it is an indication of the material bearing creep deformation [71]. Sargent–Ashby model [72] can be employed to examine the indentation creep behavior of the studied samples. According to this model the time dependent microhardness is given by the following relation:

$$H_V(t) = \frac{\sigma_0}{(\mu c \in_0 t)^{\frac{1}{\mu}}}, \tag{12}$$

where $\in_0$ is the strain rate at reference stress σ_0, c is a constant and μ is the stress exponent.

Figure 8 displays the experimental data fitted according to Sargent–Ashby model for $Zn_{1-x}Er_xO$ nano-particles samples (x = 0.02 and x = 0.10), at fixed applied loads F = 1, 5 and 10 N, respectively. From the plots of ln (H_v) against ln (t) straight lines are obtained whose slopes equivalent to the negative inverse stress exponent − 1/μ. It can be seen that the fitted lines are almost parallel; indicating that the stress exponents are not much influenced by the Er-substitutions content [73]. The values of the estimated stress exponent at applied loads F = 1, 5 and 10 N for all samples are listed in Table 4. Much information about the mechanism affecting the deformation can be revealed through the value of the stress exponent μ. If μ has a value around one this means that the sample suffers from a diffusion creep [74], for μ with value very close to two there will be a grain boundary sliding [73, 75]. For μ values in the range between 4 and 6 dislocations climbs exist [76]. However, dislocation creep is dominated if μ have values range from 3 to 10 [77, 78]. In our case of study, the relative values of μ range from 2.5 to 9.7. Thus, the studied samples possess grain boundary sliding and dislocation climbs at low loads followed by dislocation creep for higher loads within the operative creep mechanism. Moreover, according to the power law creep, a drop in stress exponent causes a rise in creep rate due to a decrease in yield strength [75, 79]. Therefore, the sample with higher stress exponent is more resistant to indentation creep compared to the other samples. In our work, at F = 1 N, erbium doping makes the samples more resistant to indentation creep till x = 0.06, then beyond this doping concentration, the resistance of the samples to indentation creep decreases as it was indicated by the values of the stress exponents. While, at F = 5 and 10 N, the samples with 6 and 8% erbium doping, respectively, show more resistance to indentation creep than the other samples since they possessed the highest values of stress exponents.

Table 4 Stress exponents for $Zn_{1-x}Er_xO$ nano-particles at constant loads for F = 1, 5 and 10 N

x	μ		
	F = 1 N	F = 5 N	F = 10 N
0.00	5.26	8.05	8.26
0.01	6.32	5.99	6.43
0.02	6.64	3.91	3.67
0.04	7.90	2.50	3.25
0.06	6.34	8.13	9.58
0.08	3.21	7.19	9.70
0.10	3.29	3.78	5.70

Sharma et al. [80] differentiated Eq. (12) with respect to time. They obtained the following form:

$$\left(\frac{1}{H_v}\right)\left(\frac{dH_v}{dt}\right) = -C_4 \in_0 \left(\frac{H_v}{\sigma_0}\right)^{\mu} \tag{13}$$

C_4 is a constant, a plot of $\ln \left[\left(-\frac{1}{H_v}\right)\left(\frac{dH_v}{dt}\right)\right]$ versus $\ln (H_v)$ at a constant temperature has a slope μ. Figure 9 displays the experimental data fitted according to Eq. 13 for $Zn_{1-x}Er_xO$ nano-particles sample (x = 0.02) at the applied load F = 10 N. It was found that the values of the stress

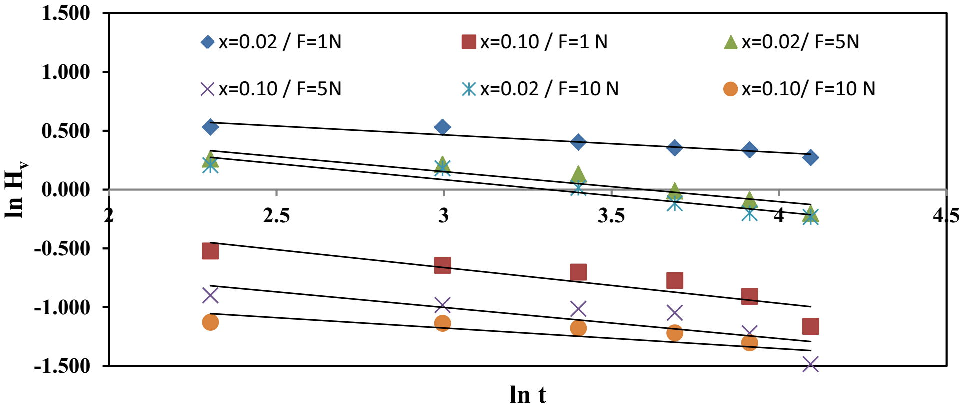

Fig. 8 Variation of $\ln(H_V)$ against ln(t) at different loads 1, 5 and 10 N for x = 0.02 and x = 0.10 samples

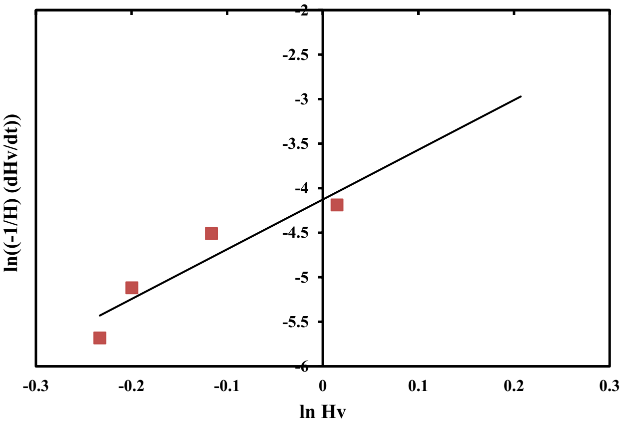

Fig. 9 Plot of $\ln\left[\left(-\frac{1}{H_v}\right)\left(\frac{dH_v}{dt}\right)\right]$ versus ln (H_v) at F = 10 N for x = 0.02 nano-sample

exponent at applied loads F = 1, 5 and 10 N for all samples estimated using the two forms of Sargent–Ashby model (Eq. 12 and 13) are almost close to each other.

4 Conclusion

Nanoparticle samples of $Zn_{1-x}Er_xO$, $0.00 \le x \le 0.10$, were successfully prepared by the wet chemical co-precipitation method. Vickers microhardness data for $Zn_{1-x}Er_xO$ showed that the variation could be analyzed into two regimes, where the microhardness values decrease with increasing the applied load and the plateau regime is reached around about 3 N for the prepared samples. Also, it was noticed that erbium doping has a noticeable influence on increasing the microhardness of ZnO nanoparticle samples up to x = 0.06. Moreover, it was observed that MPSR model was the most appropriate model for describing the load independent microhardness data of Er-doped ZnO nanoparticle samples. Indentation creep behavior of Er-doped ZnO nanoparticles showed that the samples possessed grain boundary sliding and dislocation climbs at low loads followed by dislocation creep for higher loads within the operative creep mechanism.

Acknowledgements This work has been performed in the materials science Lab, Physics Department, Faculty of Science, Beirut Arab University, Debbieh, in cooperation with Faculty of Science, Alexandria University, Alexandria, Egypt.

Compliance with ethical standards

Conflict of interest The authors declare that they have no conflict of interest.

References

1. Lee JH, Park BO (2003) Transparent conducting ZnO: Al, In and Sn thin films deposited by the sol–gel method. Thin Solid Films 426:94–99
2. Ismail B, Abaab M, Rezig B (2001) Structural and electrical properties of ZnO films prepared by screen printing technique. Thin Solid Films 383:92–94
3. Ozgur U, Alivov Y, Liu CYI, Teke A, Reshchikov M, Doğan S, Avrutin A, Cho VS-J, Morkoc H (2005) A comprehensive review of ZnO materials and devices. J Appl Phys 98:041301
4. Sahal M, Hartiti B, Ridah A, Mollar M, Marí B (2008) Structural, electrical and optical properties of ZnO thin films deposited by sol–gel method. Microelectron J 39:1425–1428
5. Das J, Khushalani D (2010) Nonhydrolytic route for synthesis of ZnO and its use as a recyclable photocatalyst. J Phys Chem C 114:2544–2550
6. Nazari M, Ghasemi N, Maddah H, Motlagh MM (2014) Synthesis and characterization of maghemite nanopowders by chemical precipitation method. J Nanostruct Chem 4:99–103
7. Kumar H, Sangwan M, Sangwan P (2013) Synthesis and characterization of MnO_2 nanoparticles using co-precipitation technique. Int J Chem Chem Eng 3:155–160
8. Bahsi Z, Oral A (2007) Effects of Mn and Cu doping on the microstructures and optical properties of sol–gel derived ZnO thin films. Opt Mater 29:672–678
9. Cheng JP, Zhang XB, Tao XY, Lu HM, Luo ZQ, Liu F (2006) Fine-tuning the synthesis of ZnO nanostructures by an alcohol thermal process. J Phys Chem B 110:10348–10353
10. Rai VK, Rai DK, Rai SB (2006) Pr^{3+} doped lithium tellurite glass as a temperature sensor. Sens Actuators A 128:14–17
11. Fedorov PP, Luginina AA, Kuznetsov SV, Osiko VV (2011) Nanofluorides. J Fluor Chem 132:1012–1039
12. Krebs JK, Feofilov SP, Kaplyanskii AA, Zakharchenya RI, Happek U (1999) Non-radiative relaxation of Yb^{3+} in highly porous γ-Al_2O_3. J Lumin 83–84:209–213
13. Tada H, Shiho O, Kuroshima K, Koyama M, Tsukamoto K (1986) An improved colorimetric assay for interleukin 2. J Immunol Methods 93:157–165
14. Alakshin EM, Blokhin DS, Sabitova AM, Klochkov AV, Klochkov VV, Kono K, Korableva SL, Tagirov MS (2012) Experimental proof of the existence of water clusters in fullerene- like PrF_3 nanoparticles. JETP Lett 96:181–183
15. Zhao S, Li P, Wei Y (2012) Effects of Ni doping on the luminescent and magnetic behaviors of ZnO nanocrystals. Powder Technol 224:390–394
16. Vidyasagar CC, Naik YA, Venkatesh TG, Viswanatha R (2011) Solid-state synthesis and effect of temperature on optical properties of Cu–ZnO, Cu–CdO and CuO nanoparticles. Powder Technol 214:337–343
17. Arda L, Açıkgöz M, Güngör A (2011) Magnetic and microstructure properties of Ni-Doped ZnO films and powder by sol–gel process. J Supercond Novel Magn 25:2701–2705
18. Muthukumaran S, Gopalakrishnan R (2012) Structural, optical and photoluminescence studies of heavily Mn-doped ZnO nanoparticles annealed under Ar atmosphere. J Mater Sci Mater Electron 23:1393–1401

19. Siddheswaran R, Mangalaraja RV, Avila RE, Manikandan D, Jeyanthi CE, Ananthakumar S (2012) Evaluation of mechanical hardness and fracture toughness of Co and Al co-doped ZnO. Mater Sci Eng A 558:456–461
20. Rajkovic V, Bozic D, Devecerski A, Jovanovic MT (2012) Characteristic of copper matrix simultaneously reinforced with nano- and micro-sized Al_2O_3 particles. Mater Charact 67:129–137
21. Shun T-T, Chang L-Y, Shiu M-H (2012) Microstructure and mechanical properties of multiprincipal component $CoCrFeNiMo_x$ alloys. Mater Charact 70:63–67
22. Arda L, Ozturk O, Asikuzun E, Ataoglu S (2013) Structural and mechanical properties of transition metals doped ZnMgO nanoparticles. Powder Technol 235:479–484
23. Soomro MY, Hussain I, Bano N, Broitman E, Nur O (2012) Willander M (2012) Nanoscale elastic modulus of single horizontal ZnO nanorod using nanoindentation experiment. Nanoscale Res Lett 7:146–148
24. Zhou J, Fei P, Gao YF, Gu YD, Liu J, Bao G, Wang ZL (2008) Mechanical–electrical triggers and sensors using piezoelectric micowires/nanowires. Nano Lett 8:2725–2730
25. Yuan QZ, Zhao YP, Li LM, Wang TH (2009) Ab initio study of ZnO-based gas-sensing mechanisms: Surface reconstruction and charge transfer. J Phys Chem C 113:6107–6113
26. Wan Q, Li QH, Chen YJ, Wang TH, He XL, Li JP, Lin CL (2004) Fabrication and ethanol sensing characteristics of ZnO nanowire gas sensors. Appl Phys Lett 84:3654–3656
27. Wang ZL, Song JH (2006) Piezoelectric nanogenerators based on zinc oxide nanowire arrays. Science 312:242–246
28. Yang RS, Qin Y, Dai LM, Wang ZL (2009) Power generation with laterally-packaged piezoelectric fine wires. Nat Nanotechnol 4:34–39
29. Westbrook JH (1953) Temperature dependence of the hardness of pure metals. Trans Am Soc Met 45:221
30. Atkins AG (1982) Topics in indentation hardness. Met Sci J 16:127–137
31. Underwood EE (1957) Creep properties from short time tests. Mater Methods 45:127
32. Geach GA (1974) Hardness and temperature. Int Met Rev 19:255–267
33. Chiang D, Li JCM (1994) Impression creep of lead. J Met Res 9:903–908
34. Lin PH, Du XH, Chen YH, Chen HC, Huang JC (2016) Nanoscaled diffusional or dislocation creep analysis of single-crystal ZnO. AIP Adv 6:095125
35. Asikuzun E, Ozturk O, Arda L, Akcan D, Senol SD, Terzioglu C (2015) Preparation, structural and micromechanical properties of (Al/Mg) co-doped ZnO nanoparticles by sol–gel process. J Mater Sci Mater Electron 26:8147–8159
36. Farhat S, Rekaby M, Awad R (2018) Synthesis and characterization of Er-doped nano ZnO samples. J Supercond Nov Magn 72:1–11
37. Coey JMD, Wongsaprom K, Alaria J, Venkatesan M (2008) Charge-transfer ferromagnetism in oxide nanoparticles. J Phys D 41:134012
38. Phan TL, Zhang YD, Yang DS, Nghia NX, Thanh TD, Yu SC (2013) Defect-induced ferromagnetism in ZnO nanoparticles prepared by mechanical milling. Appl Phys Lett 102:072408
39. Inamdar DY, Lad AD, Pathak AK, Dubenko I, Ali N, Mahamuni S (2010) Ferromagnetism in ZnO nanocrystals: doping and surface chemistry. J Phys Chem C 114:1451–1459
40. Chen WB, Liu XC, Li F, Chen HM, Zhou RW, Shi EW (2015) Influence of oxygen partial pressure on the microstructural and magnetic properties of Er-doped ZnO thin films. AIP Adv 5:067105
41. Dietl T, Ohno H, Matsukura F (2001) Hole-mediated ferromagnetism in tetrahedrally coordinated semiconductors. Phys Rev B 63:195205
42. Jayachandraiah C, Sivakumar K, Divya A, Krishnaiah G (2016) Erbium induced magnetic properties of Er/ZnO nanoparticles. AIP Conf Proc 1731:050116
43. Chikazumi S (1959) Physics of magnetism. Wiley, New York, p 187
44. Leenders A, Ullrich M, Freyhardt HC (1997) Influence of thermal cycling on the mechanical properties of VGF melt-textured YBCO. Physica C 279:173–180
45. Awad R, Aboualy AI, Kamal M, Anas M (2011) Mechanical properties of $(Cu_{0.5}Tl_{0.5})$-1223 substituted by Pr. J Supercond Nov Magn 24:1947–1956
46. Erb U (1995) Electrodeposited nanocrystals: synthesis, properties and industrial applications. Nanostruct Mater 6:533–538
47. Venkatraman R, Bravman JC (1992) Separation of film thickness and grain-boundary strengthening effects in Al thin-films on Si. J Mater Res 7:2040–2048
48. He W, Bhole SD, Chen D (2008) Modeling the dependence of strength on grain sizes in nanocrystalline materials. Sci Technol Adv Mater 9:015003
49. Armstrong RW (2016) Hall–Petch description of nanopolycrystalline Cu, Ni and Al strength levels and strain rate sensitivities. Philos Mag 96:3097–3108
50. Yen CY, Jian SR, Chen GJ, Lin CM, Lee HY, Ke WC, Liao YY, Yang PF, Wang CT, Lai YS, Jang SC, Juang JY (2011) Influence of annealing temperature on the structural, optical and mechanical properties of ALD-derived ZnO thin films. Appl Surf Sci 257:7900–7905
51. Bahadur N, Srivastava AK, Kumar S, Deepa M, Nag B (2010) Influence of cobalt doping on the crystalline structure, optical and mechanical properties of ZnO thin films. Thin Solid Films 518:5257–5264
52. Li X, Gao H, Murphy CJ, Gou LF (2004) Nanoindentation of Cu_2O nanocubes. Nano Lett 10:1903–1907
53. Roeder RK (2013) Mechanical characterization of biomaterials. In: Bandyopadhyay A, Bose SE (eds) Characterization of biomaterials. Academic Press, Oxford, pp 49–104
54. El Mustafa AA, Stone DS (2003) Nanoindentation and the indentation size effect: kinetics of deformation and strain gradient plasticity. J Mech Phys Solids 51:357–381
55. Hays C, Kendall EG (1973) An analysis of Knoop microhardness. Metallography 6:275–282
56. Bull SJ, Page TF, Yoffe EH (1989) An explanation of the indentation size effect in ceramics. Philos Mag Lett 59:281–288
57. Gong J, Wu J, Guan Z (1999) Examination of the indentation size effect in low-load Vickers hardness testing of ceramics. J Eur Ceram Soc 19:2625–2631
58. Li H, Bradt RC (1996) The effect of indentation-induced cracking on the apparent microhardness. J Mater Sci 31:1065–1070
59. Barakat MM, Abou-Aly AI, Awad R, Aly NS, Ibrahim S (2015) Mechanical properties of $Y_{3-x}Nd_xBa_{5-x}Ca_xCu_8O_{18-\delta}$ samples. J Alloys Compd 652:158–166
60. Sangwal K (2000) On the reverse indentation size effect and microhardness measurement of solids. Mater Chem Phys 63:145–152
61. Sangwal K (2009) Indentation size effect, indentation cracks and microhardness measurement of brittle crystalline solids—some basic concepts and trends. Cryst Res Technol 44:1019–1037
62. Yoda K, Sualatu Takaichi A, Nomura N, Tsutsumi Y, Doi H, Kurosu S, Chiba A, Igarashi Y, Hanawa T (2009) Effects of chromium and nitrogen content on the microstructures and mechanical properties of as-cast Co–Cr–Mo alloys for dental applications. Acta BioMater 8:2856–2862

63. Ozturk O, Asikuzun E, Kaya S, Yildirim G, Turkoz MB, Kilic A (2014) Improvement of the nature of indentation size effect of Bi-2212 superconducting matrix by doped Nd inclusion and theoretical modeling of new matrix. J Supercond Nov Magn 27:1403–1412
64. Yang T, Zang H, He C, Guo D, Zhang P, Xi J, Wang LMZ, Shen T, Pang L, Yao C (2015) Int J Appl Ceram Technol 12:390–398
65. Sahin O, Uzun O, Kolemen U, Duzgun B, Ucar N (2005) Indentation size effect and microhardness study of β-Sn single crystals. Chin Phys Lett 22:3137–3140
66. Güder HS, Sahin E, Sahin O, Göçmez H, Duran C, Çetinkara HA (2011) Vickers and Knoop indentation microhardness study of β-SiAlON ceramic. Acta Phys Pol A 120:1026–1033
67. Asikuzun E, Donmez A, Arda L, Cakiroglu O, Ozturk O, Akcan D, Tosun M, Ataoglu S, Terzioglu C (2015) Structural and mechanical properties of (Co/Mg) co-doped nano ZnO. Ceram Int 41:6326–6334
68. Anas M, Ebrahim S, Eldeen IG, Awad R, Abou-Aly AI (2017) Effect of single and multi-wall carbon nanotubes on the mechanical properties of Gd-123 superconducting phase. Chem Phys Lett 686:34–43
69. Curkovic L, Lalic M, Šolic S (2009) Analysis of the indentation size effect on the hardness of alumina ceramics using different models. Kovove Mater 47:89–93
70. Feltham P, Banerjee R (1992) Theory and application of microindentation in studies of glide and cracking in single crystals of elemental and compound semiconductors. J Mater Sci 27:1626–1632
71. Zaki HM, Abdel-Daiem AM, Swilem YI, El-Tantawy F, Al- Marzouki FM, Al-Ghamdi AA, Al-Harbi TS (2011) Indentation creep behavior and microstructure of Cu–Ge ferrites. Mater Sci Appl 2:1076–1082
72. Sargent PM, Ashby MF (1992) Indentation creep. Mater Sci Technol 8:594–601
73. Mahmudi R, Geranmayeh AR, Mahmoodi SR, Khalatbari A (2007) Room-temperature indentation creep of lead-free Sn–Bi solder alloys. J Mater Sci Mater Electron 18:1071–1078
74. Langdon TG (2000) Identifiying creep mechanisms at low stresses. Mater Sci Eng A 283:266–273
75. Walser B, Sherby OD (1982) The Structure dependence of power law creep. Scr Metall 16:213–219
76. Sharma G, Ramanujan RV, Kutty TRG, Tiwari GP (2000) Hot hardness and indentation creep studies of a Fe–28Al–3Cr–0.2C alloy. Mater Sci Eng A 278:106–112
77. Goetze C, Brace WF (1972) Laboratory observations of high-temperature rheology of rocks. Tectonophysics 13:583–600
78. Kohlstedt DL, Goetze C (1974) Low-stress high-temperature creep in olivine single crystals. J Geophys Res 79:2045–2051
79. Cseh G, Bär J, Gudladt HJ, Lendvai J, Juhasz A (1999) Indentation creep in a short fibre-reinforced metal matrix composite. Mater Sci Eng A 272:145–151
80. Sharma G, Ramanujan RV, Kutty TRG, Prabhu N (2005) Indentation creep studies of iron aluminide intermetallic alloy. Intermetallics 13:47–53